Revealing High Na-Content P2-Type Layered Oxides as Advanced Sodium-Ion Cathodes

Authors

Chenglong Zhao,[1,2†] Zhenpeng Yao,[3†] Qidi Wang,[4,5†] Haifeng Li,[6] Jianlin Wang,[7] Yaxiang Lu,[1,2*] Jordi Cabana,[6] Baohua Li,[4] Xuedong Bai,[7] Alán Aspuru-Guzik,[3,8] Marnix Wagemaker,[9*] Liquan Chen[1], and Yong-Sheng Hu[1,2,10*]

Affiliations

[1]Key Laboratory for Renewable Energy, Beijing Key Laboratory for New Energy Materials and Devices, Laboratory for Advanced Materials & Electron Microscopy, Beijing National Laboratory for Condensed Matter Physics, Institute of Physics, Chinese Academy of Sciences, Beijing 100190, China.

[2]Center of Materials Science and Optoelectronics Engineering, University of Chinese Academy of Sciences, Beijing 100049, China.

[3]Department of Chemistry and Chemical Biology, Harvard University, Cambridge, MA, 02138, USA.

[4]Division of Energy and Environment, Engineering Laboratory for the Next Generation Power and Energy Storage Batteries Graduate School at Shenzhen, Tsinghua University, Shenzhen 518055, China.

[5]School of Materials Science and Engineering Tsinghua University, Beijing 100084, China.

[6]Department of Chemistry, University of Illinois at Chicago, Chicago, Illinois 60607, United States.

[7]State Key Laboratory for Surface Physics, Institute of Physics, Chinese Academy of Sciences, Beijing, 100190, China.

[8]Department of Chemistry and Department of Computer Science, University of Toronto, Toronto, Ontario M5S 3H6, Canada and Vector Institute, Toronto, ON M5G 1M1, Canada.

[9]Department of Radiation Science and Technology, Delft University of Technology, Mekelweg 15, 2629JB Delft, the Netherlands.

[10]Yangtze River Delta Physics Research Center Co. Ltd, Liyang 213300, China.

Abstract

Sodium-ion batteries have attracted significant attention for the application in emerging grid-scale energy storage owing to the abundant Na resources and its low-cost, in which layered oxides are the subject of intensive investigation for their high structural compatibility to provide good electrochemical performance. However, the main challenge is to realize long-term cycling stability in combination with an accessible capacity, which still remains elusive, correlated with the peculiar crystal chemistry. Herein, we propose a promising P2-type material with high Na-content, $Na_{45/54}Li_{4/54}Ni_{16/54}Mn_{34/54}O_2$, where the high Na-content (~45/54 mol) usually undergoes an O3-type structure with respect to Na_xTMO_2 (TM=transition metal). Results demonstrate that this P2 material exhibits ultra-long cycle life (up to 3,000 cycles) and better rate capability (up to 3,200 mA g^{-1}). Moreover, through a multi-electron reaction of Ni^{2+}/Ni^{4+} , more than 100 mAh g^{-1} were accumulated upon first charge to 4.0 V directly, compared to ~80 mAh g^{-1} in low Na-content (~0.67 mol) materials. The origin of the favorable structure properties reveals that high Na-content P2 materials offer large potential to develop long-cycle-life Na-ion cathodes and beyond.

Introduction

Recently, sodium-ion batteries (NIBs) have gained much attention in battery field, both academic and industrial, owing to their potential application in large-scale electrical energy storage systems (EESs).(*1-3*) Significant efforts have been made in searching for suitable electrode materials with the desired properties, including high energy density, excellent cycle/rate capability, high Coulombic efficiency (CE), and favorable economic aspects. Generally, layered oxides constitute one class of suitable electrodes for NIBs due to their high structural compatibility towards Na-ion insertion, where the properties can be tailored via the introduction of various transition metal (TM) elements. Until now, several layered Na-ion electrodes have been reported, including high-capacity Mn-based (P2-$Na_{2/3}Fe_{1/2}Mn_{1/2}O_2$(*4*)) and Ni-rich (O3-Na[NiCoMn]O_2(*5*)) compounds; low-cost Cu-based (O3-$Na_{0.90}Cu_{0.22}Fe_{0.30}Mn_{0.48}O_2$(*6*)) and high-voltage Ni-based P2-$Na_{2/3}Ni_{2/3}Te_{1/3}O_2$(*7*).

Na-based layered oxides can be categorized into two main structural groups, O3- and P2-type structures, compared to layered electrodes for Li-ion batteries (LIBs), which mostly crystallize in an O3-type structure. O represents that Na ions are accommodated at the octahedral (O) sites and P denotes Na ions at trigonal prismatic (P) sites; the number 2 or 3 represents the number of edge-sharing TMO_6 octahedra with the oxygen stacking in ABBA or ABCABC packings, respectively, as shown in fig. S1 and S2.(*8*) It is noteworthy that O- and P-type oxides often experience detrimental structural transitions during the charge-discharge process, making it a challenge to realize good cycling performance. Compared to the O3-type structure, P2 frameworks enable fast Na^+ diffusion owing to the open prismatic diffusion pathways between the TMO_2 slabs.(*9, 10*) This provides the opportunity to achieve high cycle and/or rate capabilities. However, it is well established that P2-type electrodes offer a low initial charge capacity of ~80 mAh g^{-1} below 4.1 V(*4, 11, 14-21*) and an low average voltage <3.2 V(*13, 15, 19, 22*). In addition, they often suffer from a detrimental phase transition from P2 to O2, and OP4/'Z' phases upon charging, which compromises the cyclability.(*4, 11-15*)

Various methods have already been developed to improve the performance of P2-type materials. Ion-substitution and/or doping, with Li^+, Mg^{2+}, Al^{3+}, Ti^{4+}, and Zn^{2+} having no or fully occupied *d* orbitals(*11, 16, 23-26*) and Cu^{2+} inducing the Jahn-Teller effect(*15*), are widely used to alleviate the structural transitions or increase the specific capacity. Wang *et al*. used 5% Mg to substitute Ni in $Na_{2/3}Ni_{1/3}Mn_{2/3}O_2$, where the global O2 phase transition was inhibited to some extent, resulting instead in the integrated P2-O2 or 'Z' phase transition.[11] For TM^{3+}-based P2-type oxides with transition metals such as V^{3+}(*24*), Mn^{3+}(*14*),24, Fe^{3+}(*4*) and Co^{3+}(*27*) a higher initial charge capacity of >100 mAh g^{-1} below 4.1 V has been observed. However, the redox potential of these P2-type cathode materials is always lower than 3.0 V, and they often suffer from large structural transitions in both the high-voltage (P2 to O2, OP4/'Z') and low-voltage (P2 to P'2) regions. An additional disadvantage is that these TM^{3+}-based materials are often sensitive to water and moisture in the air.(*28*) The Na^+ content plays a dominant role in the structural stability of the P2 host, because Na^+ shields the electrostatic repulsions between the TMO_2 slabs. Upon desodiation the decreased shielding will drive the gliding of TMO_2 slabs, resulting in the structure transition from the P to O type configuration. Therefore, an important goal is to develop P2 materials with high Na content, so that more Na^+ to be retained in the NaO_2 slabs to prevent the structure transition, while reaching or exceeding the capacity of P2 materials with low Na content.

To gain a better insight into the performance of this kind of P2-type oxides, we aimed to prepare P2-type materials with maximized Na content and explored their properties for application as Na-ion cathodes. However, several questions must be taken into account during the materials design. What is the highest Na content in P2-type oxides and if such a material could be easily synthesized? What types of TM ions should be included to ensure a high voltage and enough charge compensation for Na^+ deintercalation? In this work, we use P2-type $Na_{2/3}Ni_{1/3}Mn_{2/3}O_2$ as a starting model to explore the potential high Na-content P2 materials.

$Na_{2/3}Ni_{1/3}Mn_{2/3}O_2$ is a typical low Na-content P2-type material, which exhibits a low initial charge capacity of ~80 mAh g^{-1} below 4.1 V, and the unwished P2 to O2 or OP4/'Z' phase transition.[26] The dichotomy example companied with the concentration gradient design was employed to search for the Na content in P2 material from 2/3 to 1 mol per unit via introducing different elements into the pristine structure, such as Li^+, Mg^{2+}, Cu^{2+}, Mn^{3+}, Fe^{3+}, and Ti^{4+}, to substitute the Mn^{4+}/Ni^{2+} partly or entirely and maintain overall charge balance of the P2-type oxides. After all of our trials, several high Na-content materials were obtained with Na concentration from 42/54 to 45/54 mol per unit.

Results

Structural analysis

In this work, a P2-type material with high Na content, $Na_{45/54}Li_{4/54}Ni_{16/54}Mn_{34/54}O_2$, was prepared based on the known P2-type $Na_{2/3}Ni_{1/3}Mn_{2/3}O_2$, and selected as the research model due to their similar components as well as the same synthesis method (see Methods). In the as-prepared material, 34/54 mol Mn ions and 16/54 mol Ni ions exist in the tetravalent state and divalent state, as in the $Na_{2/3}Ni_{1/3}Mn_{2/3}O_2$ material. The small fraction of Li ions allows an increase in Na composition by balancing the charge. Inductively coupled plasma atomic emission spectrometry (ICP-AES) analysis confirms the composition of $Na_{0.85}Li_{0.08}Ni_{0.30}Mn_{0.62}O_2$, as shown in table S1. The morphology of this as-prepared material is characterized by scanning electron microscopy (SEM), shown in fig. S3, displaying plate-like particles with a distribution of sizes in the range of 8~12 μm. The crystal structure and phase purity were evaluated by Rietveld refinement analysis of X-ray diffraction (XRD) pattern presented in Fig. 1a. All the diffraction peaks can be indexed by the hexagonal structure with the space group of $P6_3/mmc$, reflecting the disordered Ni/Mn distribution. Crystallographic data, atomic coordinates, occupancies and anisotropic displacement parameters of this structure are listed in table S2 and S3. Compared to the lattice parameters of $Na_{2/3}Ni_{1/3}Mn_{2/3}O_2$(*29*) ($a$ = 2.885 Å, c = 11.155 Å), those of $Na_{0.85}Li_{0.08}Ni_{0.30}Mn_{0.62}O_2$ (a = 2.89058(7) Å and c = 11.07541(18) Å) indicate an expanded a-b plane and a contracted c axis, originating from an increased Na^+-Na^+ electrostatic repulsions in the NaO_2 in-plane direction and an increased O^{2-}-Na^+-O^{2-} electrostatic cohesions between NaO_6 and TMO_6 polyhedra, respectively. The detailed crystal structure is further investigated by high-resolution transmission electron microscopy (HRTEM), where the interplanar distance between the adjacent lattice fringes corresponds to the d spacing value of the (002) planes of the obtained P2 phase shown in fig. S4. Na ions occupy two kinds of trigonal prismatic sites, amounting 0.536 mol in the 2d site and 0.313 in the 2b site. The prismatic NaO_6 2b site shares two faces with the lower and upper octahedral TMO_6, which can be expected to be less stable than the that 2d site which shares edges with six octahedral TMO_6 rationalizing the difference in site occupancy. The TM columns of Ni and Mn positions are revealed by the spherical aberration-corrected scanning transmission electron microscopy (STEM) shown in Fig. 1b, where both high angle annular dark-field (HAADF) and annular bright-field (ABF) images are provided for comparison. The faint bright contrast represents the Na and O columns between the octahedral TMO_2 slabs in the ABF-STEM image which is consistent with the P2-type structure as demonstrated by the inset. The distance of the adjacent layer $d_{(TM\text{-}TM)}$ in HAADF-STEM image is measured to be ~0.558 nm, which closely corresponds to the interslab distance from the XRD refinement. Atomic-scale STEM imaging and electron energy loss spectroscopy (EELS) mappings of this P2 material was carried out to confirm the elemental distribution, and the corresponding elemental mappings of Na, Mn, Ni and O are exhibited in Fig. 1c. TM sites are occupied by Mn and Ni in a disordered arrangement, while Na is located in the sites between the TMO_2 layers.

Prediction of stability of high Na-content P2-type oxide

First-principles density functional theory (DFT)(*30-32*) calculations are used to explore the high Na content in P2-type $Na_{12}LiNi_3Mn_8O_{24}$ oxide. We firstly study Li/Mn/Ni ordering in transition metal (TM) layer with a fully occupied Na layer (composition $NaLi_{1/12}Ni_{1/4}Mn_{2/3}O_2$). A P2-$NaTMO_2$ supercell with 12 metal sites was built, resulting in 910 symmetrically inequivalent configurations for Li:Ni:Mn ratio of 1:3:8. The total energies of these configurations were evaluated and the one with the lowest energy is selected as the ground state of $Na_{12}LiNi_3Mn_8O_{24}$, as shown in Fig. 2a. Using the as-identified $Na_{12}LiNi_3Mn_8O_{24}$ structure, we then explored symmetrically inequivalent Na/vacancy configurations at Na sites in the $Na_{12}LiNi_3Mn_8O_{24}$ structure for different compositions (Na/vacancy ratios). The $Na_{12-x}LiNi_3Mn_8O_{24}$-$LiNi_3Mn_8O_{24}$ convex hull (Fig. 2b) is constructed by calculating the formation energies of all configurations with respect to the end member phases. Two high Na-content phases are identified, having a Na composition of 9/12 and 10/12, which is larger than the well-known structure with a Na composition of 8/12 per super cell. The highest Na composition was further evaluated by a Na-Li-Ni-Mn-O phase diagram (in fig. S5), which demonstrates an energy of ~1.68 eV/atom lower than the combination of stable phases: $NaMnO_2$ + Li_2MnO_3 + $Na_2Mn_3O_7$ + Na_2O_2 + $NaNiO_2$. The predicted stability of the P2-type phase reflects the feasibility of preparing this material.

Electrochemical performance

As shown in Fig. 3a, this high Na-content material delivers a high capacity of ~102.3 mAh g^{-1} in the voltage range of 2.0-4.0 V, which is higher than that of ~82 mAh g^{-1} for P2-type $Na_{2/3}Ni_{1/3}Mn_{2/3}O_2$ (see fig. S4). In $Na_{2/3}Ni_{1/3}Mn_{2/3}O_2$, the initial charge capacity has been demonstrated to originate from the single electron oxidation of the Ni^{2+}/Ni^{3+} redox couple below 4.0 V.(*16*) However, the high Na-content P2-type material contains a smaller amount of Ni^{2+} (16/54 mol) compared to 1/3 mol in $Na_{2/3}Ni_{1/3}Mn_{2/3}O_2$ and nevertheless exhibits a capacity that is 1.25 times higher in the same voltage range. The rate performance was evaluated using electrodes with a large mass loading of 8-10 mg cm^{-2} from 0.1C (16 mA g^{-1}) to 20C (3,200 mA g^{-1}) as shown in Fig. 3b. When cycled at 10C the capacity retention is ~ 65% of its initial capacity, corresponding to a relatively large current density of 1,600 mA g^{-1}. After the cycling rate test up to 20C, a reversible capacity of ~100 mAh g^{-1} reached at 0.5C also indicating excellent cyclability. This is perhaps the most appealing property of the as-prepared high Na-content $Na_{45/54}Li_{4/54}Ni_{16/54}Mn_{34/54}O_2$ material, where the ultra-stable long-term cycling stability is shown in Fig. 1c, demonstrating more than 3,000 cycles with a capacity retention of >68% at a current rate of 3.0C (540 mA g^{-1}). The average capacity decay is 0.012% per cycle. More than 70% of the capacity is retained up to 2,500 cycles with a CE that approaches 100%, which was acquired in cells that were not optimized for industrial use, indicating the large application potential of this material in NIBs. To the best of our knowledge, this high Na-content P2-type material shows the best cycling performance among all reported P2-type cathodes in Na-ion batteries so far. Clearly, the present high Na-content material also shows superior electrochemical properties compared to the low Na-content materials.(*4, 11, 14-21*)

Understanding the desodiation process and charge compensation

Although a cut-off voltage over ~4.0 V will more Na^+ deintercalation from the host structure and provide a larger capacity, this usually results in the uncontrolled structural failure and electrolyte decomposition, the related issues of which remains to be further addressed. As a fundamental research, since there is sufficient Na source to be deintercalated in this $Na_{45/54}Li_{4/54}Ni_{16/54}Mn_{34/54}O_2$, a larger capacity is expected at a higher cut-off voltage. Indeed, when charged to 4.60 V, a capacity of ~150 mAh g^{-1} is obtained, corresponding to ~0.58 mol Na^+ being deintercalated (per formula unit $Na_{45/54}Li_{4/54}Ni_{16/54}Mn_{34/54}O_2$). However, it is worth noting that ~0.58 mol Na^+ is still lower than the maximum capacity that can be provided by the two-electron transfer from 16/54 (~0.296) mol Ni^{2+} to Ni^{4+}. This suggests that oxygen does not

participate in the redox reaction for the present material when charged up to 4.6 V.(*33, 34*) To examine the origin of the charge compensation during the electrochemical desodiation, the formation energy during the desodiation is evaluated as plotted in Fig. 4b and 4c. Based on the calculated formation energies the voltage is obtained, which is in good agreement with the experimentally observed curve. To obtain more insight in the redox activity, the magnetization of the Ni and O ions are determined from the DFT calculations, shown in Fig. 4d and 4e, in which the number of unpaired electrons reflect the oxidation states of the ions. Two intermediate phases are highlighted, x=5 and 7 in $Na_{10-x}LiNi_3Mn_8O_{24}$, where x=5 corresponds to charging to 4.0 V, and x=7 to 4.60 V (the cut-off voltage). Further Na-deintercalation at higher potentials are not investigated due to the limited oxidation stability of the electrolyte. The calculated magnetization of the Mn ions is shown in fig. S8, which indicates that Mn^{4+} is not participating in the redox reaction.

Upon desodiation $Na_{10-x}LiNi_3Mn_8O_{24}$ ($0 \leq x \leq 5$) the Ni magnetization first decreases from 1.78 u_B (bohr magneton) to 1.077 u_B at x=3, corresponding to the oxidation from Ni^{2+} to Ni^{3+}. Meanwhile, the O magnetization maintains a value between 0.028 and 0.112 u_B, which indicates a relative constant redox state of the O^{2-} anion. This is also reflected by the partial density of states (pDOS) of the O 2*p* and Ni 3*d* orbitals shown in Fig. 4f, in which Ni 3*d* t_{2g} orbitals have a much larger contribution to the valence band below the Fermi level (E_F) than Mn 3*d* and O 2*p* states. Further desodiation to $Na_5LiNi_3Mn_8O_{24}$ (x=5) results in a decrease in Ni magnetization to 0.965~0.073 u_B, which indicates that all Ni^{2+} ions are oxidized to Ni^{3+} and that 1/6 of the Ni^{3+} is further oxidized to Ni^{4+}. Meanwhile, O ions are still in O^{2-} state as the O magnetization retains a value between 0.002 and 0.158 u_B. Based on the above results, the desodiation results in partial oxidation of Ni^{2+} to Ni^{4+} below 4.0 V. Upon further desodiation from $Na_5LiNi_3Mn_8O_{24}$ (x=5) to $Na_3LiNi_3Mn_8O_{24}$ (x=7), about 1/12 of the O ions display an increase in magnetic moment to 0.35 u_B. However, compared to the O magnetization of 0.69 u_B in $Li_4Mn_2O_5$(*32*), an anion redox cathode material, the significantly lower 0.35 u_B in this material should not be attributed to the oxidation of O^{2-} to O^{1-}. The Ni magnetization show the opposite trend, as residual Ni^{3+} is not further oxidized but reduced. As shown in Fig. 4g, comparing the contributions of the O *2p* and Ni 3*d* t_{2g} orbitals, the latter still dominate the valence band immediately below the E_F level, which implies a preference for electron extraction from Ni during the charge process ($Na_{10-x}LiNi_3Mn_8O_{24}$, $5 \leq x \leq 7$). On the other hand, as shown in Fig. 4h, during desodiation the Ni 3*d* states and O 2*p* states increasingly overlap near the E_F level in the valence band. This suggests a small amount of electron transfer from O^{2-} to Ni^{4+}, hence reduction of Ni^{4+} reduction to low states and oxidation of O^{2-} to high states.(*35, 36*)

Soft X-ray absorption spectroscopy (XAS), which can probe the bulk material up to a depth of 1~100 nm based on the different modes(*37*), is been widely used to investigate charge compensation mechanisms of electrode materials. Ni *L*-edge spectra of partial fluorescence yield (PFY) mode measurements were carried out at different states of charge (SOCs) shown in fig. S9. The split high-energy (L_3high) and low-energy (L_3low) features of the pristine spectrum demonstrate that Ni ions are in the divalent state, consistent with previous reports.(*38*) During the desodiation process, both Ni L_3- and L_2-edge sXAS spectra shift towards higher energies, which indicates that the Ni oxidation states increases. When increasing the potential from 3.5 V to 4.0 V the L_3high and L_2high features increase further, in good agreement with those reported for Ni^{4+}.(*38, 39*) Furthermore, a delocalized hole density at the SOC corresponding to 4.60 V is found near the O orbitals surrounding Ni^{3+} and Ni^{4+}, which suggests the existence of the itinerant bands with a mixed O/Ni orbital symmetry.[49] This agrees with the decreased Ni magnetization upon desodiation from $Na_5LiNi_3Mn_8O_{24}$ (x=5) to $Na_3LiNi_3Mn_8O_{24}$ (x=7) in Fig. 4d. The features of pre-edge peak in the ligand O *K*-edge spectra can exhibit important information on the chemical bonding between ligand and TM atomic species. Generally, the pre-edge peaks in the range of 527 to 535 eV are due to the electronic transitions from the O 1*s* state to the O(2*p*)-TM(3*d*)

hybridized states, which can be further divided into a lower energy peak of the band, and a higher peak of the O(2*p*)-TM(3*d*-e_g) hybridized states. The increase of O(2*p*)-TM(3*d*-e_g) hybridized state (in fig. S10) shows that oxidization of Ni creates more holes in the antibonding e_g orbital leading to the increase of the O *K*-edge in PFY mode measurements. This is further supported by the increasing overlap of Ni 3*d* states and O 2*p* states near the E_F level during desodiation, as shown in Fig. 4h. The small amount of valence electrons in the desodiated sample promotes charge transfer from O to Ni via ligand-to-metal charge transfer in the local bonding configuration.(*40*) Furthermore, O *K*-edge spectra from surface-sensitive total electron yield measurements (TEY) demonstrate the presence of oxygen-containing decomposition products of the electrolyte and surface densification at 4.60 V. This can suppress the O(2*p*)-TM(3*d*) hybridization features for the electrodes resulting in a relative lower average valence state of Ni/Mn ions as shown in fig. S11 and S12. (*41*) Meanwhile, the Mn *L*-edge PFY results show negligible changes upon cycling, as demonstrated in fig. S12, suggesting that the Mn^{4+} ions do not participate in the charge compensation.(*42*)

Structural evolution

To explore the structural evolution of the high Na content cathode, *in-situ* XRD experiments are carried out during the charge-discharge process as shown in Fig. 5a. At the onset of desodiation, the (002) and (004) diffraction lines slightly shift to a lower angle, while (100), (102), and (103) lines move towards a higher angle. This evolution takes only place up to ~5 mAh g^{-1} charge capacity. Subsequently, (002) and (004) reflections become asymmetric and broader, and two new P2 phases (phase 2 and 3) appear upon further charging. The (002) reflection of the pristine P2 phase (phase 1) continuously shifts to lower angles, while the (002) reflections of the new P2 phases keep increasing gradually without a shift even at the end of charging at 4.60 V. The main discrepancy between these P2 phases their Na content and occupancy in the unit cell. (*43*) (*43*) (*43*) (*43*) (*43*) [43, 44, 47, 48, 55] The material charged to 4.60 V can be very well fitted with three P2-$Na_xNi_{16/54}Mn_{34/54}Li_{4/54}O_2$ phases having very similar cell parameters (as presented in fig. S14 and table S4). These three P2 phases can all be indexed in the hexagonal $P6_3/mmc$ symmetry with phase fractions of 5.1(2)%, 32.3(2)%, 62.6(2)%, and lattice parameters of a = 2.878(33) Å and c = 11.21(13) Å, a = 2.8668(4) Å and c = 11.2335(15) Å, a = 2.8135(13) Å and c = 11.2763(14) Å, respectively. The average Na content obtained from the refinement is ~0.24 mol, in good agreement with ICP results (~0.245 mol based on the normalized value of Mn). During the refinement, a relatively large 2*b* Na^+ occupation is found in Na-poor phases. This indicates that Na^+ at the 2*d* sites is preferentially deintercalated from the structure, which is should be expected based on the larger energy associated with occupying this site.(*44, 45*) Another difference is the ~3.5 % difference in volume between the Na-poor P2 phase (phase 3) and pristine phase (phase 1). In addition, a different distance between the adjacent TM layers is obtained, where the Na-poor phase 2 and 3 exhibit at the larger distance as compared to phase 1. During the desodiation process, new P2 phases with a large interlayer distance are formed and their fractions increase simultaneously. Meanwhile, the deintercalated Na comes mainly from the pristine Na-rich P2 phase. The newly formed P2 phases can be held for the stability of the materials, as opposed to the commonly reported O2, OP4/'Z' phase transition.

During Na^+ intercalation upon discharging, the coexisting Na-poor and Na-rich phases gradually recombine to a single P2 phase as shown in Fig. 5b. By fitting the XRD patterns at different charge-discharge states, see fig. S15, it becomes apparent that the (002) reflection becomes increasingly asymmetric due to a broad feature when fully discharging to 2.0 V. This could indicate a rearrangement of the P2 phase in the material. To further study the structural stability after cycling, Rietveld refinement was conducted of an electrode after 100 cycles (*ex-situ*) as shown in fig. S16. All diffraction lines can be indexed with the hexagonal structure having a space group of $P6_3/mmc$ and no additional diffraction peaks are detected. The lattice

parameters are presented table S5 and S6. In contrast to the pristine P2 $Na_{45/54}Li_{4/54}Ni_{16/54}Mn_{34/54}O_2$ material, the lattice parameter evolutions are highly reversible, which can be held for the excellent cycling stability. The evolution of the structure is also studied at different current rates, the results of which are presented in fig. S17 and the Supplementary discussion S2.

Given the large amount of Na^+ as well as facile ionic transport in this structure, excellent electrode performance can be expected for the presented high Na-content P2-type material. The Na^+ kinetics is studied by first-principles molecular dynamics (FPMD) simulations. Fig. 5c exhibits the results of the FPMD simulations for the high Na-content P2-type material where the diffusion coefficients are determined from Na^+ mean square displacements (MSDs) from simulations ranging from 600 to 1800 K (fig. S17). In Fig. 5c, the trajectories of Na^+ are displayed to illustrate the migration pathways. As expected, Na^+ migrates through the two-dimensional planes of NaO_2 layers. As compared to the low Na material (0.667 mol), the trajectories are better interconnected showing many more jumps for the present high Na-content P2 material.(*9, 16*) Fig. 5d shows the Arrhenius plot of the calculated diffusion coefficient, resulting in a very low activation energy for diffusion (~0.28 eV) and a very large room temperature diffusion coefficient ($\sim 0.55\times10^{-10}$ cm^2 s^{-1}) as compared to layered Na cathodes(*9, 10, 14, 16, 43, 46*), signifying the excellent Na^+ mobility of the present high Na content in P2-type material.

Accelerated aging measurement and full cell

To further study the chemical stability, a measurement was designed to accelerate the aging, by storing the P2-type material in air for half a year after which it was soaked in deionized water for 2 h. The XRD patterns and the electrochemical results, shown in fig. S19 and S20, indicate that the material is stable against water and air. NIBs utilizing a hard carbon anode were assembled to investigate the full cell long-term cyclability of the high Na-content P2-type cathode, having a relatively high active mass loading of approximately 8 mg cm^{-2} as shown in fig. S21-23. The electrochemical results show that the reversible capacity is above 100 mAh g^{-1} based on the mass of the cathode at a current rate of 0.1C and high average operation voltage of ~3.3 V in the voltage of 1.5-4.0 V. The full cells have excellent capacity retention, exceeding >90 % over 400 cycles at the current rate of 2.5C.

Discussion

The P2-type layered framework ensures facile Na^+ diffusion, yet the lower Na content (~2/3 mol per unit) and structural transitions of this family of electrodes compromises both charge capacity and cycle life. Therefore, developing P2 materials with high Na content is paramount for advanced NIBs. Compared to the typical modifications, such as ion doping and/or substitution, microstructure design (surface coating, morphological control), *etc.*, developing high Na-content P2-type materials presents a promising strategy, potentially providing a rich family of new cathode materials. The findings on the present high Na-content P2-type material provides several advantages that may be achieved by this type of materials.

Promoting oxidization of the low-valent cations (*e.g.,* Ni^{2+}) to their valence high states even for a relatively low cut-off charge voltage. For $Na_{45/54}Li_{4/54}Ni_{16/54}Mn_{34/54}O_2$, the Ni^{2+}/Ni^{4+} redox couple is successfully activated, providing a high-capacity even below 4.0 V, which is an essential ingredient for the design of high-performance Ni-based P2-type cathodes. Generally, Ni^{2+} to Ni^{4+} redox occurs at voltages exceeding 4.2 V. Such a higher redox potential introduces two disadvantages, structural transitions and activation of the oxygen redox potentially leading to oxygen loss. Both will degrade the performance of cathode materials in terms of capacity and structural stability. Introducing a large amount of Na (0.75~0.83 mol per unit) into the P2-type material results in a lower average oxidation state of the TM ions as compared to low Na-content

(~0.67 mol) P2 materials. The low TM oxidation state in high Na content P2 materials can increase the contribution of low-valent cations in valence band below the Fermi level to provide electron transfer. To rationalize this finding, DFT calculations were performed as shown in Fig. 6a. We compare the pDOS of two P2-type materials $Na_{0.83}Li_{1/12}Ni_{1/4}Mn_{2/3}O_2$ and $Na_{0.67}Li_{1/12}Ni_{1/4}Mn_{2/3}O_2$ with average oxidation states of TM ions in +3.167 and +3.333, respectively, where the former displays a larger contribution near the Fermi level. This implies easier participation of Ni^{2+} in the charge compensation. On the other hand, the high Na-content P2 phase is less stable than that the low Na-content material as demonstrated in Fig. 2b, due to the stronger Na^+-Na^+ electrostatic repulsions within NaO_2 slabs (which may also contribute to the easier oxidation of Ni^{2+} to Ni^{4+} at low voltages). Recently, many disordered rock salt-type oxides have been explored as cathodes for Li-ion batteries, where, indeed, most of these materials are thermodynamically metastable, offering a higher capacity.(*32, 47*)

Realizing a stable P2 structure that prevents degradation through phase transitions. The large amount of Na in the P2-type host structure can ensure a high structural stability in a large compositional range during the desodiation, as demonstrated in Fig. 6b. For low Na P2 materials, structural transitions from P2 to O2 or OP4/'Z' occur for voltages below ~4.2 V when the Na composition in the crystal host drops below 1/3 mol Na. The higher Na content allows to maintain more Na^+ in the interlayers when the same amount of Na is deintercalated, which suppresses the phase transition. A smaller amount of Na in the NaO_2 slabs lowers TM^{n+}-TM^{n+} and Na^+-TM^{n+} electrostatic repulsions, resulting in gliding of the TMO_2 slabs, which induces the undesired phase transitions, leading to large volumetric changes and rapid capacity decay. Our results demonstrate that during desodiation of $Na_{45/54}Li_{4/54}Ni_{16/54}Mn_{34/54}O_2$, Na-poor phases have a similar structure as the pristine material. These newly formed phases have a larger interlayer distance compared to that of the pristine structure, which is expected to be beneficial for Na^+ migration. The phase fractions of these desodiated phases increases upon charging, and reversible transform back to the pristine structure upon discharging (sodiation) as illustrated in Fig. 6b.

Summary

In this work, we have explored the peculiar structural chemistry of high Na-content P2-type oxide as Na-ion cathodes. As a proof of concept, a high Na-content material of $Na_{45/54}Li_{4/54}Ni_{16/54}Mn_{34/54}O_2$ has been successfully prepared. This material shows a higher reversible capacity of 100 mAh g^{-1} with the promising multi-electron reaction from Ni^{2+}/Ni^{4+} redox couple in a stable electrochemical window between 2.0 to 4.0 V. More importantly, this material shows an ultra-long cycle life up to 3,000 cycles with good rate performance. The underlying origins reveal that high Na-content can promote the oxidization of low-valent cations to high redox states at a low cut-off voltage during charge, and stabilize the structure without degradation or phase transitions. The advantages of the presently developed high Na-content P2-type material highlights the importance to further explore high Na-content electrode materials for NIBs, most likely opening new opportunities and understanding. Possible dopant/substituting elements that may enable alternative high Na-content P2-type materials are multi-valent elements (*e.g.*, Ca^{2+}, Mg^{2+}, Y^{3+}, La^{3+}), which located at the Na sites will also promote the oxidation of TM ions and stabilize the structure during the charge and discharge process. The present study also reveals a promising strategy to realize multi-electron transfer toward a high oxidation state, potentially relevant in fields beyond energy storage, *e.g.,* catalysts.

Materials and Methods

Sample synthesis.

The resulting materials, $Na_{45/54}Li_{4/54}Ni_{16/54}Mn_{34/54}O_2$ and $Na_{2/3}Ni_{1/3}Mn_{2/3}O_2$ were prepared by a solid-state reaction. The stoichiometric precursors of $NaNO_3$ (>98%), NiO (>98%), MnO_2 (99%) and Li_2CO_3 (99.5%) were thoroughly mixed in an agate mortar and pressed into pellets under

pressure of 10 MPa, which was further calcined at 950-1050 ºC for 24 h with an intermediate grinding and cooled to room temperature naturally. After the heat treatment, the material was directly put into an Ar-filled glovebox to prevent any moisture exposition. Hard carbon anode was prepared according to our previous report, where the obtained samples were carbonized at 1400 °C for 3 h in a tube furnace under argon flow with a heating rate of 3°C min^{-1}.(*48*)

Materials characterizations.

Powder X-ray diffraction (XRD) was performed using a Bruker D8 Advance diffractometer equipped with a Cu Kα radiation source (λ_1=1.54060 Å, λ_2=1.54439 Å) and a LynxEye_XE detector. Rietveld refinement of the XRD was carried out using the General structure analysis system (GSAS) software with the EXPGUI software interface.(*49*) High-resolution transmission electron microscopy (HR-TEM) images and scanning transmission electron microscopy (STEM) image and electron energy loss spectroscopy (EELS) mappings were obtained using a 300kV aberration-corrected (S)TEM (JEM-ARM300F, JEOL Ltd) operated at 300kV with a cold field-emission gun and double dodeca-poles Cs correctors. The convergence angle was 18mrad and the angular range of collected electrons for high-angle annular dark field (HAADF) imaging is about 54-220mrad. The morphologies of the materials were investigated using a scanning electron microscope (Hitachi S-4800). The stoichiometry of the as-synthesized compound was determined measured by inductively coupled plasma atomic emission spectrometry (ICP-AES). In the *in-situ* XRD studies, the working electrode was prepared using PVDF as binder on an Al foil. A specially designed Swagelok cell equipped with an X-ray transparent Al window was used for the *in-situ* measurements on charge and discharge. Mn/Ni *L*-edge and O *K*-edge X-ray absorption spectroscopy (XAS) were performed for pristine and cycled samples in the electron (surface) and fluorescence yield (bulk) modes at beamline 4-ID-C of the Advanced Photon Source. Samples were transferred from a glovebox into a transfer container and then an X-ray absorption chamber via an argon environment. This was done in order to maintain a clean sample. During the measurement, Sr_2RuO_4, MnO and Ni metal were used as standards for the energy calibration of O *K*-edge, Mn L-edge and Ni L-edge, respectively. The spectra were processed using the Athena software package.(*50*)

Electrochemical measurement.

The cathodes were prepared via mixing 80 *wt.*% active material with 10 *wt.* % acetylene black and 10 *wt.* % polyvinylidene fluoride (PVdF) on Al foil with the loading mass of the active material was about 8-10 mg cm^{-2}. The anodes were prepared via mixing 80 *wt.*% active material with 10 *wt.*% conductive additives (acetylene black: super P = 8:2) and 10 *wt.*% sodium alginate binder on Cu foil with the loading mass of the active material was 1.6~2 mg cm^{-2}. The prepared electrodes were dried at 100 ºC under vacuum for 12 h and then were fabricated into CR2032 coin-type cells with pure sodium foil as the counter electrode in an argon-filled glove box (H_2O, O_2 < 0.1 ppm). A glass fiber was used as the separator, and 0.2 M $NaPF_6$ and 0.8 M $NaClO_4$ in ethylene carbonate/diethyl carbonate (EC/DEC = 4:6 in volume) with fluoroethylene carbonate (5% in volume) was used as the electrolyte. The charge and discharge measurements were carried out on a Land BT2000 battery test system (Wuhan, China) under room temperature.

Accelerated aging measurement.

In order to check the water stabilities of the electrode materials, the as-synthesized materials were first placed in deionized water with pH values of 7 for 2 h. Then, the materials were separated from the solution and dried in an oven at 100 ºC for overnight. Note that this is an extreme condition which will never be happened for practical materials process. However, this result can reflect the stability of the material against water in a short time.

Computational methods.

All first-principles DFT calculations reported in this study were performed using the Vienna Ab-initio Simulation Package (VASP)(*51-53*) with the projector augmented wave (PAW) potentials(*54*) and the Perdew-Becke-Ernzerhof (PBE)(*55*) exchange-correlation. A plane wave

basis with a cutoff energy of 520 eV and ***Γ***-centered *k*-meshes with a density of 8000 *k*-points per reciprocal atom were used for all calculations. All calculations were spin-polarized, with Mn atoms initialized in a high-spin configuration and relaxed to self-consistency with the ferromagnetic (FM) configurations applied. The DFT + *U* method introduced by Dudarev *et al.*(*56*) was used to treat the localized 3*d* electrons of Mn, Ni with a *U* of 3.8 and 6.1 eV, obtained by fitting it to experimental and calculated formation enthalpies in a previous study(*57*).

The average sodiation/desodiation voltage can be computed using the negative of the reaction free energy per Na added/removed, as shown

$$V = \frac{\Delta G_{\mathrm{f}}}{\mathrm{F}\Delta N_{\mathrm{Na}}}$$

where F is the Faraday constant, ΔN_{Na} is the amount of Na added/removed, and ΔG_{f} is the (molar) change in free energy of the reaction. Considering a two-phase reaction between $\mathrm{Na_x TMO}$ and $\mathrm{Na_y TMO}$, $\mathrm{Na_x TMO} + (y-x)Na \rightarrow \mathrm{Na_y TMO}$, ΔG_{f} can be approximated by the total internal energies from DFT calculations neglecting the entropic contributions (T = 0 K)

$$\Delta E = E(\mathrm{Na_x TMO}) - E\left(\mathrm{Na_y TMO}\right) - (y-x)E(\mathrm{Li_{metal}})$$

where $E(\mathrm{Na_x TMO})$ and $E\left(\mathrm{Na_y TMO}\right)$ are the DFT energies at the respective compositions. The neglect of entropic contributions means that the lithiation voltage profiles will follow the T = 0 K ground-state convex hull and consist of a series of constant voltage steps along the two-phase regions of the convex hull, separated by discontinuities that indicate the single-phase compounds on the hull. It is worth mentioning here that, in practice, sodiation/desodiation do not necessarily proceed through two-phase reactions. Thus, the calculated T = 0 K voltage profiles should be viewed as an approximation to the actual voltage profiles(*58*). At finite temperatures (for example, room temperature), the "steps" in the voltage profile became more rounded because of entropic effects(*51*).

The first-principles molecular dynamics (FPMD) calculations is used to investigate the Na ions transport properties in this high Na-content P2-type oxide. This FPMD simulations are carried out for 10 ps at each temperature by a Nose-Hoover thermostat, and a time step of 1 fs is used to integrate the equation of motion, where the ***Γ*** point is used for the Brillouin zone in order to keep the computational cost at a reasonable level. The ionic diffusion behavior in this system is calculated by a time-dependent mean square displacement (MSD),

$$\mathrm{MSD}(t) = \langle r^2(t)\rangle = \langle |r_i(t) - r_i(0)|^2\rangle$$

where $r_i(t)$ is the position of the i-th Na^+ at the time t, and the average is over the time steps and all the Na^+. According to the Einstein equation, the slope of the MSD presents the diffusion coefficient D,

$$D = \frac{1}{6}\lim_{t\to\infty}\frac{d}{dt}\langle r^2(t)\rangle$$

therefore, the activation energy barrier for Na^+ diffusion can be extracted from the diffusion coefficients at various temperatures according to Arrhenius equation.

Supplementary Materials

Fig. S1. Crystal structure of the O3 type oxide in the Rhombohedral structure with the space group of *R*-3*m* (166).

Fig. S2. Crystal structure of the P2 type oxide in the hexagonal structure with the space group of *P*6$_3$/*mmc* (193).

Fig. S3. Scanning electron microscope (SEM) image of this high Na-content P2-type $Na_{45/54}Ni_{16/54}Mn_{34/54}Li_{4/54}O_2$ compound.

Fig. S4. High-resolution transmission electron microscope (HRTEM) image of this high Na-content P2-type $Na_{45/54}Ni_{16/54}Mn_{34/54}Li_{4/54}O_2$ compound**.**

Fig. S5. Evaluation the stability of the $Na_{5/6}Li_{1/12}Ni_{1/4}Mn_{2/3}O_2$ phase in the Na-Li-Ni-Mn-O chemical space.

Fig. S6. Galvanostatic charge-discharge curves of $Na_{2/3}Ni_{1/3}Mn_{2/3}O_2$ at a rate of 0.15C in the voltage range of 2.0 and 4.0 V *vs.* Na^+/Na.
Fig. S7. Cycling stability of $Na_{45/54}Ni_{16/54}Mn_{34/54}Li_{4/54}O_2$ with first three cycles at 0.1C and following at 3.0C in the voltage ranges of 2.0-4.0 V *vs.* Na^+/Na.
Fig. S8. The magnetization and oxidation state evolution during the desodiation process of Mn ions in intermediate phases from $Na_{5/6}Li_{1/12}Ni_{1/4}Mn_{2/3}O_2$ to $Li_{1/12}Ni_{1/4}Mn_{2/3}O_2$.
Fig. S9. Ni *L*-edge X-ray absorption spectra (XAS) of electrochemically cycled $Na_{45/54}Ni_{16/54}Mn_{34/54}Li_{4/54}O_2$ electrodes in partial fluorescence yield (PFY) mode.
Fig. S10. O *K*-edge XAS spectra of electrodes cycled to different states of charge (SOCs) using PFY mode.
Fig. S11. O *K*-edge XAS spectra of electrodes cycled to different SOCs using total electron yield (TEY) mode.
Fig. S12. Ni and Mn *L*-edge XAS spectra of electrodes cycled to different SOCs using TEY mode.
Fig. S13. Mn *L*-edge XAS spectra of electrodes cycled to different SOCs using PFY mode.
Fig. S14. XRD Rietveld refinement of the electrochemically oxidized $Na_{\sim 0.25}Ni_{16/54}Mn_{34/54}Li_{4/54}O_2$ sample.
Fig. S15. LeBail refinements of *in-situ* XRD patterns at different charge-discharge states of pristine, charged to 4.0 V, and discharged to 2.0 V.
Fig. S16. Rietveld refinement of *ex-situ* X-ray diffraction (XRD) pattern of $Na_{45/54}Ni_{16/54}Mn_{34/54}Li_{4/54}O_2$ (a = 2.87831(19) Å, c = 11.1629(11) Å) after 100 cycles, and the inset showing the enlarged pattern of (002) peak.
Fig. S17. Structural evolution under electrochemical Na^+ deintercalation to 4.0 V under different charged rates.
Fig. S18. Mean square displacement (MSD) curves for each kind of ions in $Na_{5/6}Li_{1/12}Ni_{1/4}Mn_{2/3}O_2$.
Fig. S19. XRD patterns of the samples after stored half of a year **a** and soaked in neutral water for 2h **b**.
Fig. S20. Electrochemical performance of high Na-content P2 type cathode after soaked in neutral water for 2h.
Fig. S21. Electrochemical performance of hard carbon anode.
Fig. S22. Galvanostatic charge-discharge curves of high Na-content P2-type cathode $Na_{45/54}Ni_{16/54}Mn_{34/54}Li_{4/54}O_2$//hard carbon full cells.
Fig. S23. Cycling stability of high Na-content P2-type cathode $Na_{45/54}Ni_{16/54}Mn_{34/54}Li_{4/54}O_2$//hard carbon full cells.
Table S1. Stoichiometry from the inductively coupled plasma atomic emission spectrometry (ICP-AES) analysis.
Table S2. Crystallographic and Rietveld refinement data of the as-prepared $Na_{54/54}Li_{4/54}Ni_{16/54}Mn_{34/54}O_2$ compound.
Table S3. Atomic coordinates, occupancies and isotropic displacement parameters ($Å^2$).
Table S4. Crystallographic and Rietveld refinement data of the sample charged to 4.5 V.
Table S5. Crystallographic and Rietveld refinement data of the sample after 100 cycles.
Table S6. Atomic coordinates, occupancies and isotropic displacement parameters ($Å^2$) after 100 cycles.

References and Notes

1. B. Dunn, H. Kamath, J.-M. Tarascon, Electrical Energy Storage for the Grid: A Battery of Choices. *Science* **334**, 928 (2011).

2. J.-Y. Hwang, S.-T. Myung, Y.-K. Sun, Sodium-ion batteries: present and future. *Chemical Society Reviews* **46**, 3529-3614 (2017).
3. M. Á. Muñoz-Márquez, D. Saurel, J. L. Gómez-Cámer, M. Casas-Cabanas, E. Castillo-Martínez, T. Rojo, Na-Ion Batteries for Large Scale Applications: A Review on Anode Materials and Solid Electrolyte Interphase Formation. *Advanced Energy Materials* **7**, 1700463 (2017).
4. N. Yabuuchi, M. Kajiyama, J. Iwatate, H. Nishikawa, S. Hitomi, R. Okuyama, R. Usui, Y. Yamada, S. Komaba, P2-type Nax[Fe1/2Mn1/2]O2 made from earth-abundant elements for rechargeable Na batteries. *Nat Mater* **11**, 512-517 (2012).
5. J.-Y. Hwang, S.-M. Oh, S.-T. Myung, K. Y. Chung, I. Belharouak, Y.-K. Sun, Radially aligned hierarchical columnar structure as a cathode material for high energy density sodium-ion batteries. *Nature Communications* **6**, 6865 (2015).
6. L. Mu, S. Xu, Y. Li, Y.-S. Hu, H. Li, L. Chen, X. Huang, Prototype Sodium-Ion Batteries Using an Air-Stable and Co/Ni-Free O3-Layered Metal Oxide Cathode. *Advanced Materials* **27**, 6928-6933 (2015).
7. A. Gupta, C. Buddie Mullins, J. B. Goodenough, Na2Ni2TeO6: Evaluation as a cathode for sodium battery. *Journal of Power Sources* **243**, 817-821 (2013).
8. C. Delmas, C. Fouassier, P. Hagenmuller, Structural classification and properties of the layered oxides. *Physica B+C* **99**, 81-85 (1980).
9. Y. Wang, R. Xiao, Y.-S. Hu, M. Avdeev, L. Chen, P2-Na0.6[Cr0.6Ti0.4]O2 cation-disordered electrode for high-rate symmetric rechargeable sodium-ion batteries. *Nature Communications* **6**, 6954 (2015).
10. N. A. Katcho, J. Carrasco, D. Saurel, E. Gonzalo, M. Han, F. Aguesse, T. Rojo, Origins of Bistability and Na Ion Mobility Difference in P2- and O3-Na2/3Fe2/3Mn1/3O2 Cathode Polymorphs. *Advanced Energy Materials* **7**, 1601477 (2017).
11. P.-F. Wang, Y. You, Y.-X. Yin, Y.-S. Wang, L.-J. Wan, L. Gu, Y.-G. Guo, Suppressing the P2–O2 Phase Transition of Na0.67Mn0.67Ni0.33O2 by Magnesium Substitution for Improved Sodium-Ion Batteries. *Angewandte Chemie International Edition* **55**, 7445-7449 (2016).
12. E. Talaie, V. Duffort, H. L. Smith, B. Fultz, L. F. Nazar, Structure of the high voltage phase of layered P2-Na2/3−z[Mn1/2Fe1/2]O2 and the positive effect of Ni substitution on its stability. *Energy & Environmental Science* **8**, 2512-2523 (2015).
13. B. Mortemard de Boisse, D. Carlier, M. Guignard, L. Bourgeois, C. Delmas, P2-NaxMn1/2Fe1/2O2 phase used as positive electrode in Na batteries: structural changes induced by the electrochemical (de)intercalation process. *Inorg Chem* **53**, 11197-11205 (2014).
14. G. Singh, N. Tapia-Ruiz, J. M. Lopez del Amo, U. Maitra, J. W. Somerville, A. R. Armstrong, J. Martinez de Ilarduya, T. Rojo, P. G. Bruce, High Voltage Mg-Doped Na0.67Ni0.3–xMgxMn0.7O2 (x = 0.05, 0.1) Na-Ion Cathodes with Enhanced Stability and Rate Capability. *Chemistry of Materials* **28**, 5087-5094 (2016).
15. L. Zheng, J. Li, M. N. Obrovac, Crystal Structures and Electrochemical Performance of Air-Stable Na2/3Ni1/3–xCuxMn2/3O2 in Sodium Cells. *Chemistry of Materials* **29**, 1623-1631 (2017).
16. P.-F. Wang, H.-R. Yao, X.-Y. Liu, Y.-X. Yin, J.-N. Zhang, Y. Wen, X. Yu, L. Gu, Y.-G. Guo, Na⁺/vacancy disordering promises high-rate Na-ion batteries. *Science Advances* **4**, eaar6018 (2018).
17. Y.-E. Zhu, X. Qi, X. Chen, X. Zhou, X. Zhang, J. Wei, Y. Hu, Z. Zhou, A P2-Na0.67Co0.5Mn0.5O2 cathode material with excellent rate capability and cycling stability for sodium ion batteries. *Journal of Materials Chemistry A* **4**, 11103-11109 (2016).

18. E. de la Llave, P. K. Nayak, E. Levi, T. R. Penki, S. Bublil, P. Hartmann, F.-F. Chesneau, M. Greenstein, L. F. Nazar, D. Aurbach, Electrochemical performance of Na0.6[Li0.2Ni0.2Mn0.6]O2 cathodes with high-working average voltage for Na-ion batteries. *Journal of Materials Chemistry A* **5**, 5858-5864 (2017).
19. M. H. Han, E. Gonzalo, N. Sharma, J. M. López del Amo, M. Armand, M. Avdeev, J. J. Saiz Garitaonandia, T. Rojo, High-Performance P2-Phase Na2/3Mn0.8Fe0.1Ti0.1O2 Cathode Material for Ambient-Temperature Sodium-Ion Batteries. *Chemistry of Materials* **28**, 106-116 (2015).
20. L. Li, H. Wang, W. Han, H. Guo, A. Hoser, Y. Chai, X. Liu, Understanding Oxygen Redox in Cu-Doped P2-Na0.67Mn0.8Fe0.1Co0.1O2 Cathode Materials for Na-Ion Batteries. *Journal of The Electrochemical Society* **165**, A3854-A3861 (2018).
21. C. Zhao, Q. Wang, Y. Lu, L. Jiang, L. Liu, X. Yu, L. Chen, B. Li, Y.-S. Hu, Decreasing transition metal triggered oxygen redox activity in Na-deficient oxides. *Energy Storage Materials*, (2018).
22. S. M. Kang, J. H. Park, A. Jin, Y. H. Jung, J. Mun, Y. E. Sung, Na+/Vacancy Disordered P2-Na0.67Co1-xTixO2: High-Energy and High-Power Cathode Materials for Sodium Ion Batteries. *ACS Appl Mater Interfaces* **10**, 3562-3570 (2018).
23. R. J. Clément, J. Xu, D. S. Middlemiss, J. Alvarado, C. Ma, Y. S. Meng, C. P. Grey, Direct evidence for high Na+ mobility and high voltage structural processes in P2-Nax[LiyNizMn1−y−z]O2 (x, y, z ⩽ 1) cathodes from solid-state NMR and DFT calculations. *Journal of Materials Chemistry A* **5**, 4129-4143 (2017).
24. X. H. Zhang, W. L. Pang, F. Wan, J. Z. Guo, H. Y. Lu, J. Y. Li, Y. M. Xing, J. P. Zhang, X. L. Wu, P2-Na2/3Ni1/3Mn5/9Al1/9O2 Microparticles as Superior Cathode Material for Sodium-Ion Batteries: Enhanced Properties and Mechanisam via Graphene Connection. *ACS Appl Mater Interfaces* **8**, 20650-20659 (2016).
25. X. Wu, G. L. Xu, G. Zhong, Z. Gong, M. J. McDonald, S. Zheng, R. Fu, Z. Chen, K. Amine, Y. Yang, Insights into the Effects of Zinc Doping on Structural Phase Transition of P2-Type Sodium Nickel Manganese Oxide Cathodes for High-Energy Sodium Ion Batteries. *ACS Appl Mater Interfaces* **8**, 22227-22237 (2016).
26. K. Kubota, S. Kumakura, Y. Yoda, K. Kuroki, S. Komaba, Electrochemistry and Solid-State Chemistry of NaMeO2 (Me = 3d Transition Metals). *Advanced Energy Materials* **8**, 1703415 (2018).
27. R. Berthelot, D. Carlier, C. Delmas, Electrochemical investigation of the P2-NaxCoO2 phase diagram. *Nat Mater* **10**, 74-80 (2011).
28. V. Duffort, E. Talaie, R. Black, L. F. Nazar, Uptake of CO2 in Layered P2-Na0.67Mn0.5Fe0.5O2: Insertion of Carbonate Anions. *Chemistry of Materials* **27**, 2515-2524 (2015).
29. J. M. Paulsen, R. A. Donaberger, J. R. Dahn, Layered T2-, O6-, O2-, and P2-Type A2/3[M‘2+1/3M4+2/3]O2 Bronzes, A = Li, Na; M‘ = Ni, Mg; M = Mn, Ti. *Chemistry of Materials* **12**, 2257-2267 (2000).
30. Q. Bai, L. Yang, H. Chen, Y. Mo, Computational Studies of Electrode Materials in Sodium-Ion Batteries. *Advanced Energy Materials* **8**, 1702998 (2018).
31. K. Kang, Y. S. Meng, J. Bréger, C. P. Grey, G. Ceder, Electrodes with High Power and High Capacity for Rechargeable Lithium Batteries. *Science* **311**, 977 (2006).
32. Z. Yao, S. Kim, J. He, V. I. Hegde, C. Wolverton, Interplay of cation and anion redox in Li4Mn2O5; cathode material and prediction of improved Li4(Mn,M)2O5 electrodes for Li-ion batteries. *Science Advances* **4**, eaao6754 (2018).
33. X. Rong, E. Hu, Y. Lu, F. Meng, C. Zhao, X. Wang, Q. Zhang, X. Yu, L. Gu, Y.-S. Hu, H. Li, X. Huang, X.-Q. Yang, C. Delmas, L. Chen, Anionic Redox Reaction-Induced High-Capacity and Low-Strain Cathode with Suppressed Phase Transition. *Joule*, (2018).

34. C. Zhao, Q. Wang, Y. Lu, Y.-S. Hu, B. Li, L. Chen, Review on anionic redox for high-capacity lithium- and sodium-ion batteries. *Journal of Physics D: Applied Physics* **50**, 183001 (2017).
35. X. Wang, G. Liu, T. Iwao, M. Okubo, A. Yamada, Role of Ligand-to-Metal Charge Transfer in O3-Type NaFeO2–NaNiO2 Solid Solution for Enhanced Electrochemical Properties. *The Journal of Physical Chemistry C* **118**, 2970-2976 (2014).
36. D. Asakura, M. Okubo, Y. Mizuno, T. Kudo, H. Zhou, K. Amemiya, F. M. F. de Groot, J.-L. Chen, W.-C. Wang, P.-A. Glans, C. Chang, J. Guo, I. Honma, Electron delocalization in cyanide-bridged coordination polymer electrodes for Li-ion batteries studied by soft x-ray absorption spectroscopy. *Physical Review B* **84**, 045117 (2011).
37. F. Lin, D. Nordlund, I. M. Markus, T.-C. Weng, H. L. Xin, M. M. Doeff, Profiling the nanoscale gradient in stoichiometric layered cathode particles for lithium-ion batteries. *Energy & Environmental Science* **7**, 3077-3085 (2014).
38. R. Qiao, L. A. Wray, J.-H. Kim, N. P. W. Pieczonka, S. J. Harris, W. Yang, Direct Experimental Probe of the Ni(II)/Ni(III)/Ni(IV) Redox Evolution in LiNi0.5Mn1.5O4 Electrodes. *The Journal of Physical Chemistry C* **119**, 27228-27233 (2015).
39. C. Piamonteze, F. M. F. de Groot, H. C. N. Tolentino, A. Y. Ramos, N. E. Massa, J. A. Alonso, M. J. Martínez-Lope, Spin-orbit-induced mixed-spin ground state in $R\mathrm{Ni}{\mathrm{O}}_{3}$ perovskites probed by x-ray absorption spectroscopy: Insight into the metal-to-insulator transition. *Physical Review B* **71**, 020406 (2005).
40. J. Hong, W. E. Gent, P. Xiao, K. Lim, D.-H. Seo, J. Wu, P. M. Csernica, C. J. Takacs, D. Nordlund, C.-J. Sun, K. H. Stone, D. Passarello, W. Yang, D. Prendergast, G. Ceder, M. F. Toney, W. C. Chueh, Metal–oxygen decoordination stabilizes anion redox in Li-rich oxides. *Nature Materials* **18**, 256-265 (2019).
41. R. Qiao, J. Liu, K. Kourtakis, M. G. Roelofs, D. L. Peterson, J. P. Duff, D. T. Deibler, L. A. Wray, W. Yang, Transition-metal redox evolution in LiNi0.5Mn0.3Co0.2O2 electrodes at high potentials. *Journal of Power Sources* **360**, 294-300 (2017).
42. C. Ma, J. Alvarado, J. Xu, R. J. Clément, M. Kodur, W. Tong, C. P. Grey, Y. S. Meng, Exploring Oxygen Activity in the High Energy P2-Type Na0.78Ni0.23Mn0.69O2 Cathode Material for Na-Ion Batteries. *Journal of the American Chemical Society* **139**, 4835-4845 (2017).
43. Y. Wang, X. Yu, S. Xu, J. Bai, R. Xiao, Y. S. Hu, H. Li, X. Q. Yang, L. Chen, X. Huang, A zero-strain layered metal oxide as the negative electrode for long-life sodium-ion batteries. *Nat Commun* **4**, 2365 (2013).
44. M. Roger, D. J. P. Morris, D. A. Tennant, M. J. Gutmann, J. P. Goff, J. U. Hoffmann, R. Feyerherm, E. Dudzik, D. Prabhakaran, A. T. Boothroyd, N. Shannon, B. Lake, P. P. Deen, Patterning of sodium ions and the control of electrons in sodium cobaltate. *Nature* **445**, 631 (2007).
45. Y. S. Meng, Y. Hinuma, G. Ceder, An investigation of the sodium patterning in NaxCoO2 ($0.5 \leqslant x \leqslant 1$) by density functional theory methods. *The Journal of Chemical Physics* **128**, 104708 (2008).
46. S. M. Kang, J.-H. Park, A. Jin, Y. H. Jung, J. Mun, Y.-E. Sung, Na+/Vacancy Disordered P2-Na0.67Co1–xTixO2: High-Energy and High-Power Cathode Materials for Sodium Ion Batteries. *ACS Applied Materials & Interfaces* **10**, 3562-3570 (2018).
47. N. Yabuuchi, M. Takeuchi, M. Nakayama, H. Shiiba, M. Ogawa, K. Nakayama, T. Ohta, D. Endo, T. Ozaki, T. Inamasu, K. Sato, S. Komaba, High-capacity electrode materials for rechargeable lithium batteries: Li3NbO4-based system with cation-disordered rocksalt structure. *Proceedings of the National Academy of Sciences* **112**, 7650 (2015).

48. C. Zhao, Q. Wang, Y. Lu, B. Li, L. Chen, Y.-S. Hu, High-temperature treatment induced carbon anode with ultrahigh Na storage capacity at low-voltage plateau. *Science Bulletin* **63**, 1125-1129 (2018).
49. S. C. Vogel, gsaslanguage: a GSAS script language for automated Rietveld refinements of diffraction data. *Journal of Applied Crystallography* **44**, 873-877 (2011).
50. B. Ravel, M. Newville, ATHENA, ARTEMIS, HEPHAESTUS: data analysis for X-ray absorption spectroscopy using IFEFFIT. *Journal of Synchrotron Radiation* **12**, 537-541 (2005).
51. C. Wolverton, A. Zunger, First-Principles Prediction of Vacancy Order-Disorder and Intercalation Battery Voltages in LixCoO2. *Physical Review Letters* **81**, 606-609 (1998).
52. G. Kresse, J. Hafner, Ab initio molecular-dynamics simulation of the liquid-metal--amorphous-semiconductor transition in germanium. *Physical Review B* **49**, 14251-14269 (1994).
53. G. Kresse, J. Furthmüller, Efficient iterative schemes for ab initio total-energy calculations using a plane-wave basis set. *Physical Review B* **54**, 11169-11186 (1996).
54. P. E. Blöchl, Projector augmented-wave method. *Physical Review B* **50**, 17953-17979 (1994).
55. J. P. Perdew, M. Ernzerhof, K. Burke, Rationale for mixing exact exchange with density functional approximations. *The Journal of Chemical Physics* **105**, 9982-9985 (1996).
56. S. L. Dudarev, G. A. Botton, S. Y. Savrasov, C. J. Humphreys, A. P. Sutton, Electron-energy-loss spectra and the structural stability of nickel oxide: An LSDA+U study. *Physical Review B* **57**, 1505-1509 (1998).
57. L. Wang, T. Maxisch, G. Ceder, Oxidation energies of transition metal oxides within the GGA+U framework. *Physical Review B* **73**, 195107 (2006).
58. M. K. Y. Chan, C. Wolverton, J. P. Greeley, First Principles Simulations of the Electrochemical Lithiation and Delithiation of Faceted Crystalline Silicon. *Journal of the American Chemical Society* **134**, 14362-14374 (2012).

Acknowledgments

Funding: This work was supported by the National Key Technologies R&D Program, China(2016YFB0901500), the National Natural Science Foundation of China (51725206, 51421002), the Strategic Priority Research Program of the Chinese Academy of Sciences (XDA21070500), Beijing Natural Science Fund-Haidian Original Innovation Joint Fund (L182056), and the Supported by Beijing Natural Science Foundation (L182056), the Center for Electrochemical Energy Science, an Energy Frontier Research Center funded by the U.S. Department of Energy (DOE), Office of Science, Basic Energy Science (DE-AC02-06CH11357), the National Science Foundation under Grant No. DMR-1809372, and the Netherlands Organization for Scientific Research (NWO) under the VICI grant nr. 16122. C. Zhao also thanks to the State Scholarship Fund of China Scholarship Council (CSC).

Author contributions: Y.-S.H. and M.W. provided the direction and advice for the study. C.Z., Z.Y., and Q.W. conceived the study. C.Z. and Q.W. performed all synthesis procedures, experimental investigation, software programing to process and presented collected data; Z.Y. and A. A.-G. conceived the DFT calculations of the ground-state structure prediction, structural pathway, voltage, and stability analysis. J.W. and X.B. performed STEM observation and analysis with C.Z.; H.L. and J.C., performed soft XAS measurements and analysis with C.Z.; C.Z., Q.W., Z.Y., M.W. and Y.-S.H. wrote the manuscript. All authors participated in the discussion to improve the manuscript. C.Z., Z.Y., and Q.W. contributed equally to this work.

741
742 **Competing interests:** The author declares no competing financial interest.
743
744 **Data and materials availability:** All data is available in the main text or the supplementary
745 materials.
746

Figures

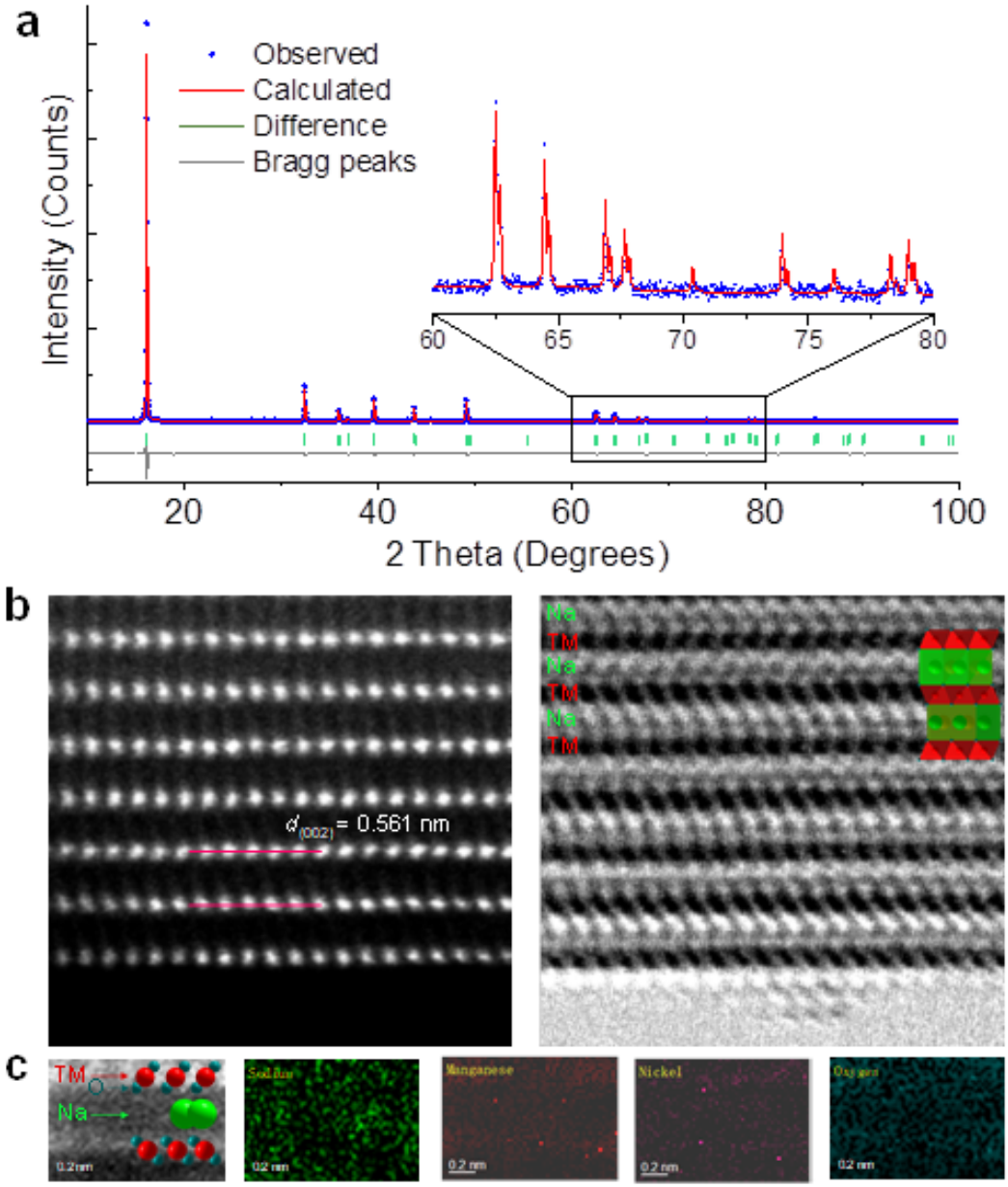

Fig. 1. Structural characterization of the high Na-content P2 type oxide. a, Rietveld refinement of X-ray diffraction (XRD) pattern of $Na_{45/54}Li_{4/54}Ni_{16/54}Mn_{34/54}O_2$ (a = 2.89058(7) Å, c = 11.07541(18) Å), and the inset showing the enlarged pattern of (002) peak. **b**, Atomic-resolution high-angle annular dark field (HAADF) and annular bright field (ABF)-scanning transmission electron microscopy (STEM) images at the [010] zone axis. **c**, Electron energy loss spectroscopy (EELS) mappings of Na, Mn, Ni, and O elements.

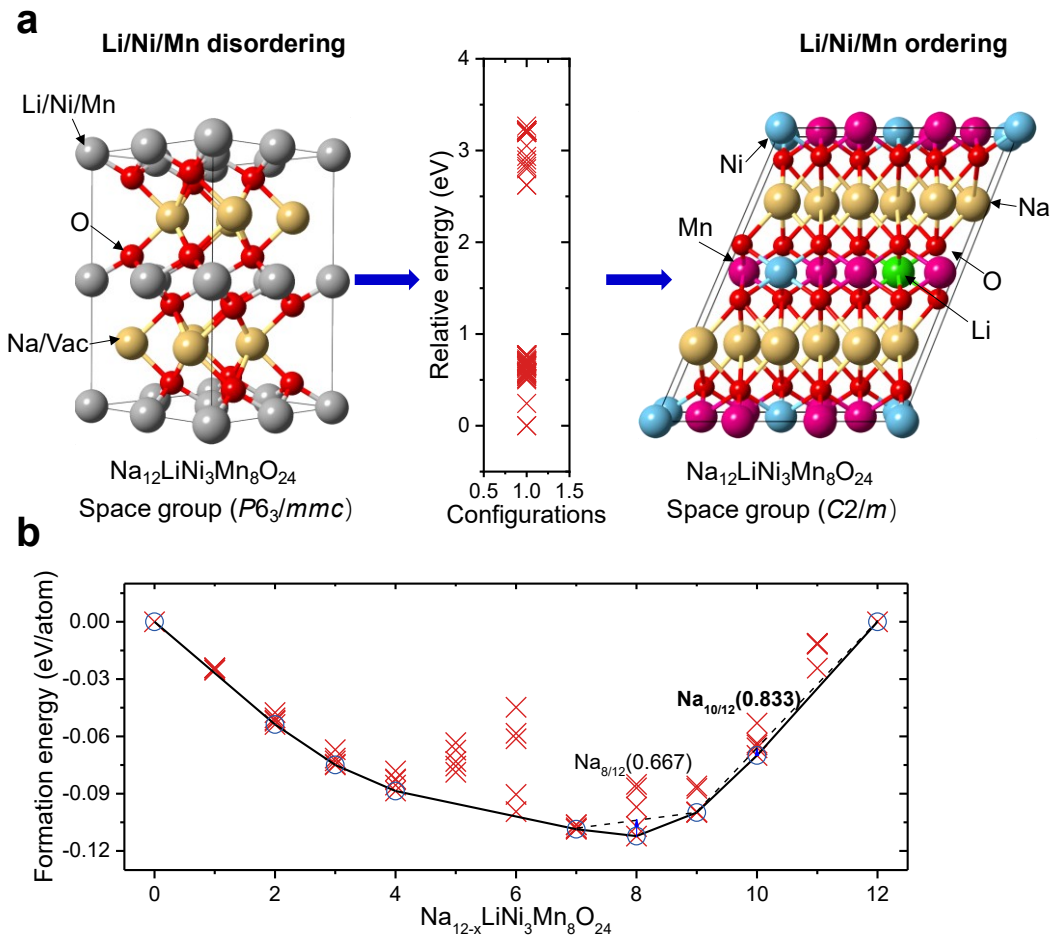

Fig. 2. Determination the Na/vacancy ordering and phase stability in convex hull. a, Determination of the Li/Ni/Mn (dis)ordering in the system of $Na_{12-x}LiNi_3Mn_8O_{24}$. The detailed information of determination on the ground state structure and Li/Ni/Mn (dis)ordering in the system of $Na_{12-x}LiNi_3Mn_8O_{24}$ is presented in the Supporting discussion S1. **b**, Phase stability in $Na_{12-x}LiNi_3Mn_8O_{24}$-$LiNi_3Mn_8O_{24}$ convex hull. The formation energy was calculated considering all possible Na and their vacancy configurations, and the potential structures with different Na contents were predicted in this study. Red crosses indicate the energies of different enumerated phases computed at the Na content. Blue circles are ground states, as they are part of the convex energy hull in solid line.

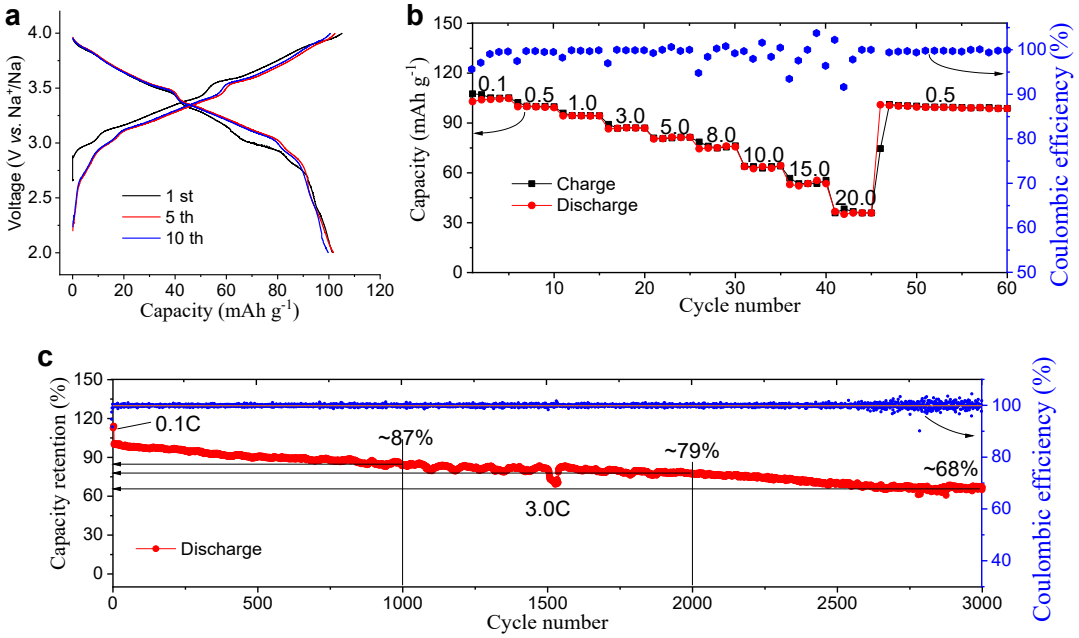

Fig. 3. Electrochemical performance of high Na-content P2 type cathode of $Na_{45/54}Li_{4/54}Ni_{16/54}Mn_{34/54}O_2$. **a**, Galvanostatic charge-discharge curves of electrode at a rate of 0.15C (corresponding to ~22 mA g^{-1}) in the voltage range of 2.0-4.0 V *vs.* Na^+/Na. **b**, Rate capability from 0.1C (16 mA g^{-1}) to 20C (3,200 mA g^{-1}). **c**, Discharge capacity retention of with first the three cycles at 0.1C (18 mA g^{-1}) and following cycled at 3.0C (540 mA g^{-1}). The capacity is normalized by that of 3.0C. Above 70 % capacity is retained up to 2,500 cycles with approximate 100% Coulombic efficiency (CE), but the CE is found to be unstable in the following cycles; after 3,000 cycles, ~68% capacity is remained (see fig. S7 for the details).

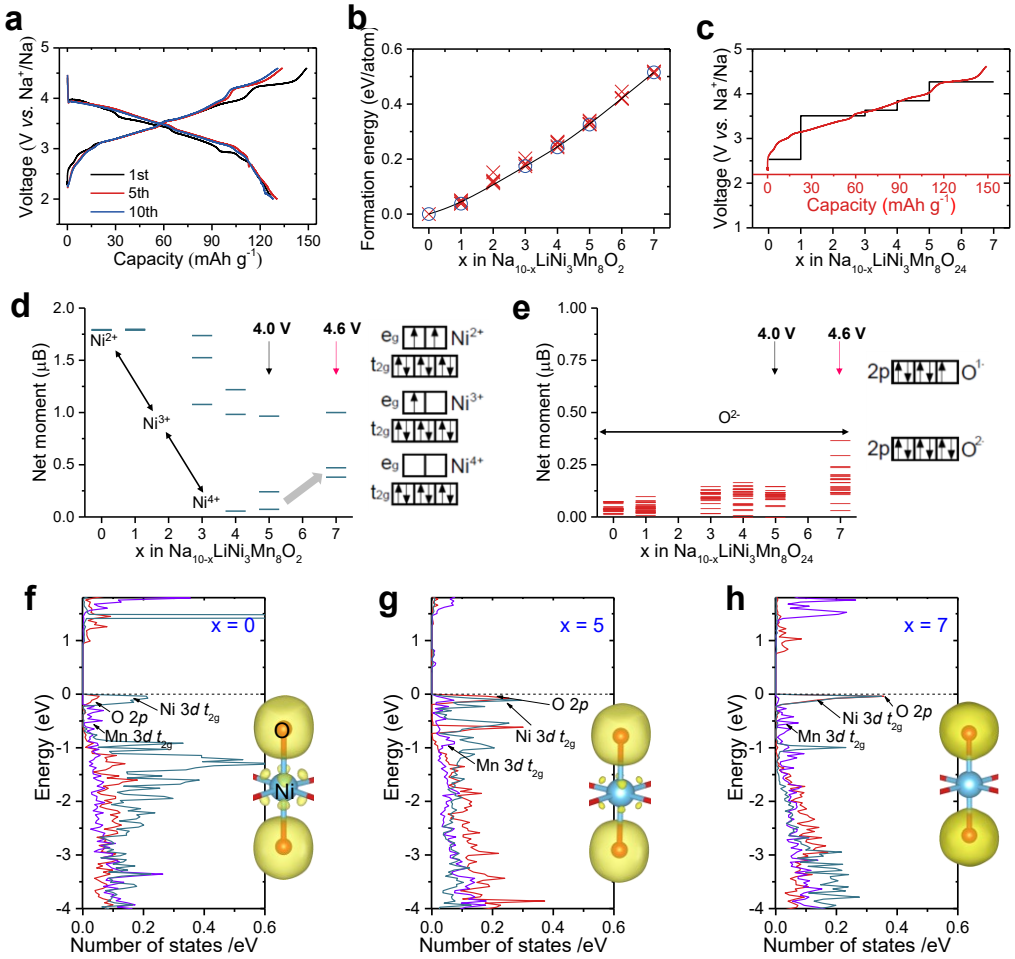

Fig. 4. The desodiation process and redox sequence during the first charging process. **a**, Galvanostatic charge-discharge curves of $Na_{45/54}Ni_{16/54}Mn_{34/54}Li_{4/54}O_2$ at a rate of 0.15C in the voltage range of 2.0-4.60 V. **b** and **c**, The calculated formation energy of desodiation structures of $Na_{10-x}LiNi_3Mn_8O_{24}$ ($0 \leq x \leq 7$) convex hull and the corresponding voltage profile during the desodiation process in $Na_{45/54}Li_{4/54}Ni_{16/54}Mn_{34/54}O_2$. **d** and **e**, The magnetization and oxidation state evolution during the desodiation process of Ni and O ions in intermediate phases from $Na_{10}LiNi_3Mn_8O_{24}$ to $Na_3LiNi_3Mn_8O_{24}$. Electronic structure evolution on partial density of states (pDOS) of the Ni 3*d* t_{2g}, Mn 3*d* t_{2g} and O 2*p* orbitals of the x=0 (**f**), 5 (**g**), and 7 (**h**) in $Na_{10-x}LiNi_3Mn_8O_{24}$. The Fermi energy is set to 0 eV. Insets show the iso-surface of the charge density for the lowest unoccupied states of different desodiated states.

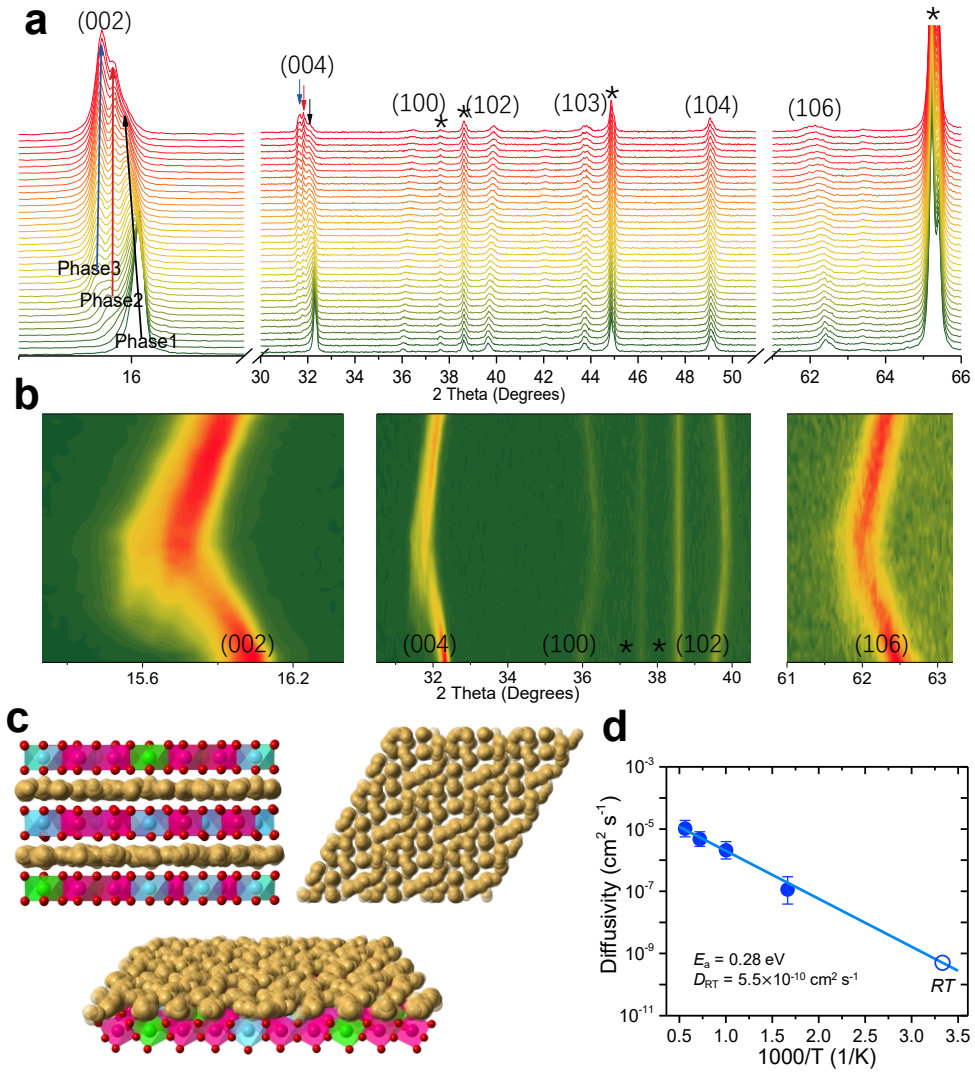

Fig. 5. Structural evolution and Na^+ ion transport properties of this P2-type cathode. **a**, *In-situ* XRD patterns recorded at a rate of 0.05C charged to 4.60 V. The peaks marked by an asterisk is from the case of *in-situ* Swagelok cell. **b,** *In-situ* XRD patterns recorded at a high rate of 0.5C in voltage range of 2.0-4.0 V. **c**, Pathway of Na^+ migration in this high Na-content P2-type oxide simulated at a temperature of at ~1400 K from a period of 6 ps. The detailed views of Na^+ layers are given in the right and below panels, where the yellow spheres indicate the trace of Na^+ positions during MD simulations. **d**, Arrhenius plot of diffusion coefficients, from which the Na^+ ion migration energy barrier of 0.28 eV is obtained in a low temperature range from the room temperature (RT) to 1800 K.

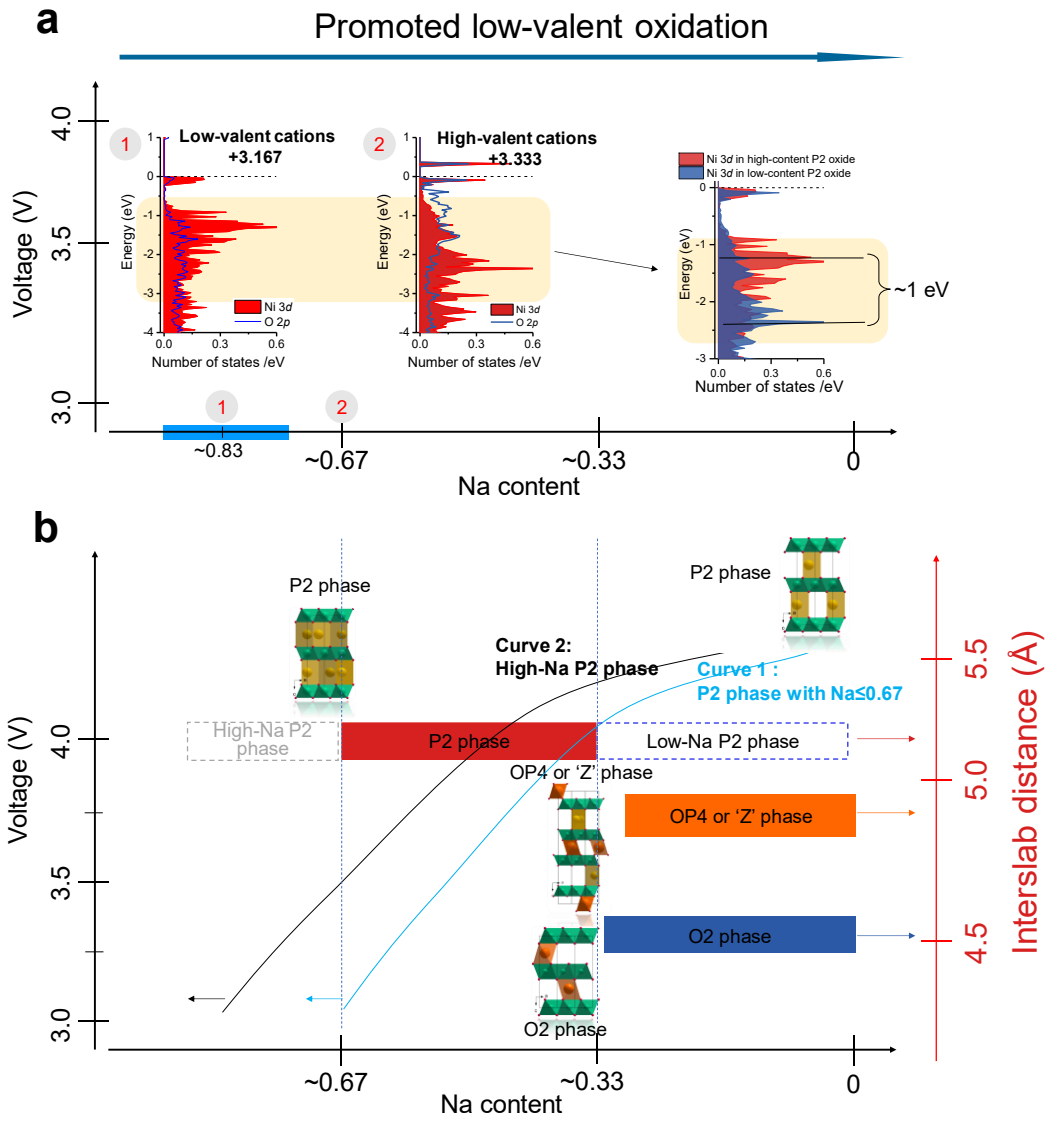

Fig. 6. Illustration of the electronic and structural evolution mechanism in this high Na-content P2-type material of $Na_{45/54}Li_{4/54}Ni_{16/54}Mn_{34/54}O_2$. a, The electronic evolution during the charge process. The large amount of Na in P2-type materials makes the average oxidation state of the TM ions lower than that of commonly low Na-content P2 materials. The low-valent cations can be oxidized to the much higher states easily. **b**, Structural evolution mechanism of $Na_{45/54}Li_{4/54}Ni_{16/54}Mn_{34/54}O_2$ during the desodiation process.